Retrieving Land Surface Temperature from Satellite Imagery with a Novel Combined Strategy

María Sánchez-Aparicio *, Paula Andrés-Anaya, Susana Del Pozo (ID) **and Susana Lagüela** (ID)

Department of Cartographic and Land Engineering, University of Salamanca, Hornos Caleros, 50, 05003 Ávila, Spain; 70265257g@usal.es (P.A.-A.); s.p.aguilera@usal.es (S.D.P.); sulaguela@usal.es (S.L.)
* Correspondence: mar_sanchez1410@usal.es; Tel.: +34-920-353-505

check for
updates

Abstract: Land surface temperature (LST) is a key parameter for land cover analysis and for many fields of study, for example, in agriculture, due to its relationship with the state of the crop in the evaluation of natural phenomena such as volcanic eruptions and geothermal areas, in desertification studies, or in the estimation of several variables of environmental interest such as evapotranspiration. The computation of LST from satellite imagery is possible due to the advances in thermal infrared technology and its implementation in artificial satellites. For example, Landsat 8 incorporates Operational Land Imager(OLI) and Thermal InfraRed Sensor(TIRS)sensors the images from which, in combination with data from other satellite platforms (such as Terra and Aqua) provide all the information needed for the computation of LST. Different methodologies have been developed for the computation of LST from satellite images, such as single-channel and split-window methodologies. In this paper, two existing single-channel methodologies are evaluated through their application to images from Landsat 8, with the aim at determining the optimal atmospheric conditions for their application, instead of searching for the best methodology for all cases. This evaluation results in the development of a new adaptive strategy for the computation of LST consisting of a conditional process that uses the environmental conditions to determine the most suitable computation method.

Keywords: land surface temperature; single-channel; Landsat 8; temperature retrieval; thermal infrared

1. Introduction

In recent decades, climate change and global warming have become two of the main social, economic, and political concerns, so it is common to see news and scientific articles that show the consequences of these phenomena. For example, recent studies have shown that the average surface temperature between 2000 and 2016 was 1 °C higher than that obtained between 1975 and 2000 [1].

This rise in the average temperature of the earth is one of the main consequences of climate change, which has caused, for example, the increase in the melting rate of the poles and glaciers with a consequent rise in sea and ocean levels [2].

However, the thaw is not the only consequence of global warming, but extreme weather conditions, such as floods, hurricanes, heat waves, etc., are also increasing. For example, in the case of Spain, 2017 was one of the driest years since 1965 [3] due to a 20% decrease in rainfall, while the mean annual temperature was 1.1 °C higher than the mean temperature value for the period 1981–2010 [4]. Given the problems caused by global warming, it is logical to look for solutions. In this regard, it is key to identify, geolocate, quantify, and monitor this phenomenon.

The quantification of the earth's surface temperature, thereafter named land surface temperature (LST), is not only useful to study global warming but also to deduce the health status of agricultural crops [5], evaluate the gravity of forest fires and the state of dryness of the forest [6,7],

assess the potential of geothermal areas [8,9], or estimate the evapotranspiration of vegetated areas for different environmental studies.

The increase in earth surface temperature is a global dilemma as indicated by one of the sustainable development goals (SDGs) promoted by the United Nations [10]. Thus, monitoring this phenomenon in order to assess changes through time is key and should be performed in any part of the earth for large geographical areas. This is possible due to remote sensing satellite imagery. In fact, remote sensing is positioned as the main alternative for quantification and monitoring of the LST [11].

There are different approaches developed to calculate LST from satellite imagery using the thermal infrared (IR) spectrum. The difference between them lays on the amount and type of data used by their algorithms, especially on whether the algorithm includes the computation of the surface emissivity parameter or if it is introduced as a measured parameter [12]. In order to calculate LST, surface emissivity (also known as land surface emissivity (LSE)) can be known or unknown. In the latter, different methods are used as follows: (1) stepwise retrieval methods, such as the classification-based emissivity method (CBEM) [13]; (2) methods for simultaneous retrieval of LST and LSE with known atmospheric parameters, such as grey-body emissivity (GBE) [14] and the temperature emissivity separation (TES) algorithms [15]; and (3) methods for simultaneous retrieval of LST, LSE, and atmospheric profile, as done by artificial neural networks (ANNs) [16]. If the LSE is known, the existing methods differ on the number of IR thermal bands used. Thus, for the case of using a single IR thermal band, single-channel methods based on the resolution of the radiative transfer equation and the Planck equation are applied [17]. These methods attenuate the scarce terrain information by introducing several atmospheric parameters, such as indirect measurements of air temperature and humidity [18]. On the other hand, for the case of using more than one thermal band, split window [17] or multi-angle [19] algorithms are applied. These methods differ in the way input data is required. Split window requires differential absorption data while multi-angle requires imagery acquired at different viewing angles. All these methods require additional atmospheric corrections. These corrections can be based on images, as in the case of DOS correction [17], or on the modelling of the atmosphere, as in the codes of radiative transfer 6S [20] or MODTRAN [21].

Since 2018, the United States Geological Survey has proposed a systematic treatment for all American states named Landsat Analysis Ready Data (ARD), a 30-m spatial resolution LST product from Landsat 8 and the United States area [22]. In this regard, there are no direct LST products available anywhere else in the world with the same spatio-temporal resolutions. Regarding the most similar options, the European Space Agency has launched daily LST products as Level 2 data from Sentinel 3 satellites [23], but their spatial resolution is 1000 m, 33 times lower than data from Landsat 8. In the Sentinel 3 case, the methodology used is split-window based, thus being applicable only to sensors acquiring TIR (Thermal InfraRed) data in several bands, while ARD LST data is calculated with single-channel methodology. ASTER sensors also acquire TIR data and allow for the generation of an LST product with a resolution of 90 m. On the other hand, ASTER sensors from NASA and the Japan Ministry of Economy, Trade, and Industry offer this product for specific data collections [24] without a real global coverage.

Thus, this paper aims to find the optimal atmospheric conditions for the application of two existing single-channel methods for estimating LST from Landsat 8 data, but applicable to other satellite platforms, to reproduce this result anywhere in the world. For this reason, the Landsat ARD LST product is considered as a reference to evaluate the results obtained with the strategy proposed. In addition, the fact that the ARD LST products have been widely evaluated and validated reinforces their use as reference products [25,26].

Based on this, the present work seeks to make an in-depth study of the existing single-channel methodologies for computing LST based on satellite thermal data. It differs from similar works, such as [27], in the fact that the focus is set on the development of an adaptive strategy to apply the best methodology based on the atmospheric conditions of each case study, instead of searching for the best method in a general way. In this case, Landsat 8 and MODIS sensors onboard Terra were

chosen, but the process can be extrapolated to any other satellite sensor that offers thermal, visible, and near-infrared data, such as ASTER. The results support the possibility of applying a combined strategy, which selects automatically the appropriate method based on the environmental conditions of each pixel.

1.1. LST Retrieval Methods

There are two different types of methodologies to calculate LST from satellite images, as shown in Figure 1; on the one hand, there are methods that use previously "known" or rather approximate emissivity, and on the other hand, there are methods that consider emissivity as unknown [12].
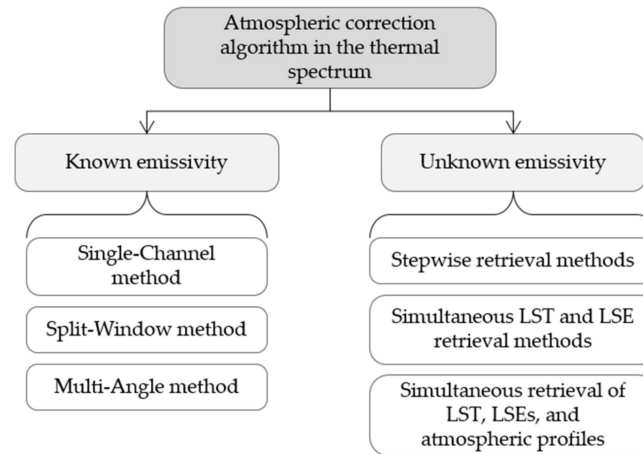

Figure 1. Diagram of the different methods to obtain the terrestrial surface temperature from satellite images. LST is land surface temperature; LSE is land surface emissivity.

This paper focuses only on those methods in which emissivity was previously known, and more specifically on single-channel methods. The reason for working with these methods was the fact that they can be applied to many different satellites, from those that acquire in only one range of the thermal IR band, to those that acquire images in two or more bands in the thermal IR range. When working with Landsat 8 in this article, the use of thermal band 10 was recommended, since band 11 presented problems in its calibration as indicated by different investigations [18].

1.2. Single-Channel Methods

Single-channel methods include those that use a single thermal band. In our case studies in which the Landsat 8 satellite was used, band 10 was chosen.

Within the single-channel methods there were two different methodologies considered in this paper:

Direct inversion of the radiative transfer equation: the radiative transfer equation and the Planck equation are known, such that

$$L_{sensor\ i} = \tau_i \Big[\varepsilon_i B_i(T_s) + (1 - \varepsilon_i) L^{\downarrow}_{atm\ i} \Big] + L^{\uparrow}_{atm\ i} \tag{1}$$

where

$$B_i(T_s) = \frac{2hc^2}{\lambda_i^5 * \left(e^{\frac{hc}{\lambda_i k T_s}} - 1 \right)} \tag{2}$$

$$T_S = \frac{C_1}{\lambda_i ln \left(\frac{C_2}{\lambda_i^5 \frac{L_{sensor\ i} - L^{\uparrow}_{atm\ i} - \tau_i (1 - \varepsilon_i) L^{\downarrow}_{atm\ i}}{\tau_i \varepsilon_i}} + 1 \right)} \tag{3}$$

being:

$L_{sensor i}$: the spectral radiance obtained by the sensor, measured in $W \cdot m^2 \cdot sr^{-1} \cdot \mu m^{-1}$.
$B_i (T_s)$: the measured radiance if the surface were a black body at the surface temperature T_s.
τ_i: the total transmissivity of the atmosphere for the channel I of the sensor.
ε_i: the surface emissivity.
$L^{\downarrow}_{atm\ i}$: the ascending atmospheric radiance.
$L^{\uparrow}_{atm\ i}$: the descending atmospheric radiance.
λ: the wavelength of the band i.
k: the Boltzmann constant, $k = 1.3806 \times 10^{-23}$ $m^2 \cdot kg/s^2 \cdot K$.
h: the Planck constant, $h = 6.6261 \times 10^{-34}$ $m^2 \cdot kg/s$.
c: the speed of light in a vacuum, $c = 2.9979 \cdot 108$ m/s.
C_1: the first radiation constant equivalent to $1.19104 \cdot 10^8$ $W \cdot \mu m^4/m^2 \cdot sr$. It is calculated from $C_1 = 2\pi \cdot h \cdot c^2$.
C_2: the second radiation constant calculated as $C_2 = h \cdot c/k$ with a value of $1.4388 \cdot 10^4$ K·m.

In this case it would be necessary to know the emissivity of the earth's surface and the different atmospheric parameters: transmissivity and atmospheric radiance both ascending and descending. These parameters can be obtained from atmospheric profiles and radiative transfer codes. As an example of the first, there are radiosoundings, reanalysis, and satellite sounders [28]. In the case of radiative transfer models, some examples are MODTRAN, RTTOV, and ATCOR [21].

Generalized Single-Channel Algorithm: These algorithms were developed to simplify the radiative transfer equation. An attempt was made to avoid dependence on atmospheric profiles due to the fact that they are not always available or are too complex to acquire, and instead algorithms were developed that use other atmospheric parameters such as water vapor or air temperature. The original algorithm that all single-channel methods have in common was developed in [29], and its formula is as follows:

$$Ts = \gamma \left[\varepsilon^{-1} (\psi_1 \cdot L_{sensor\ i} + \psi_2) + \psi_3 \right] + \delta \qquad (4)$$

where Υ and δ, the parameters obtained from the Planck function, are defined as follows:

$$\gamma = \left[\frac{C_2 \cdot L_{sensor\ i}}{Tb^2_{sensor\ i}} \left[\frac{\lambda^4}{C_1} L_{sensor\ i} + \lambda^{-1} \right] \right]^{-1} \qquad (5)$$

$$\delta = -\gamma \cdot L_{sensor\ i} + Tb_{sensor\ i}. \qquad (6)$$

Tb: Brightness temperature in the sensor in Kelvin (K).
ψ_1, ψ_2, and ψ_3: the atmospheric functions.

The values of these last functions are the difference from one method to the other. For this paper the generalized single-channel algorithm was used. There are many single-channel algorithms, but two of them are exposed in detail, for which they are called single-channel 1 and single-channel 2, the main difference of which lays in the atmospheric functions used.

1.2.1. Single-Channel 1

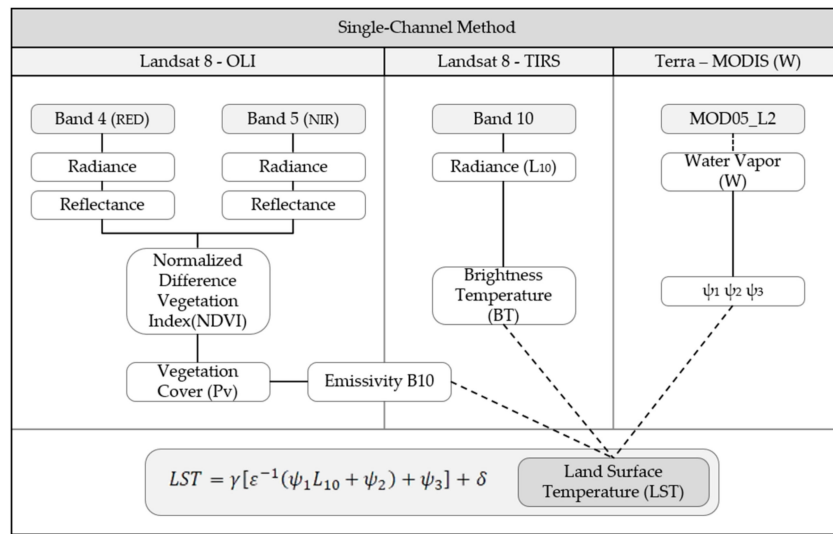This method is based on [17], with the pipeline shown in Figure 2.

Figure 2. Working scheme of the single-channel method for Landsat 8 images.

To execute this method, four different images are needed:

- Image of the red band (0.62–0.70 μm). Band 4 for Landsat 8.
- Image of the near infrared band (0.75–1.10 μm). Band 5 for Landsat 8.
- Image of the infrared thermal band (10.00–15.00 μm). Band 10 for Landsat 8.
- Preprocessed products of column water vapor (W) given in g/cm^2. For this article, products of the MODIS sensor were used, specifically of the Terra satellite, since this follows a similar path to that of Landsat 8, with an approximate lag of 30 minutes. Specifically, the MOD05_L2 product was used [30].

For the single-channel 1 method, the values of the atmospheric functions were obtained with a second degree polynomial in which the water vapor content is related, since, as indicated previously, this is one of the parameters with higher contribution to the atmospheric effect in the region of the thermal infrared.

$$\begin{bmatrix} \psi_1 \\ \psi_2 \\ \psi_3 \end{bmatrix} = \begin{bmatrix} 0.04019 & 0.02916 & 1.01523 \\ -0.3833 & -1.50294 & 0.20324 \\ 0.00918 & 1.36072 & -0.27514 \end{bmatrix} \begin{bmatrix} W^2 \\ W \\ 1 \end{bmatrix} \tag{7}$$

According to [17], LST errors for this method become unacceptable for high water vapor contents (for contents greater than 2.5 g/cm^2). It also indicates that this problem can be solved by including air temperature as an input, as was done in more recent works [29].

1.2.2. Single-Channel 2

The working scheme is the same as for the single-channel 1 method, so the same inputs were needed.

The difference is that this method was based on [21] and works with a third-degree polynomial to obtain the atmospheric functions. The original method published in [31] but corrected for Landsat 8 was analyzed in this paper. Therefore, the atmospheric functions in this case are

$$\psi_k = \eta_{k\lambda} W^3 + \xi_{k\lambda} W^2 + \chi_{k\lambda} W + \varphi_{k\lambda}$$
$$\text{Where}: \ k \ = \ 1, \ 2, \ 3 \tag{8}$$

The atmospheric functions incorporate spectral functions, which are defined for each wavelength as shown in Table 1.

Table 1. Table of spectral functions to obtain the values of atmospheric functions from the wavelength of the thermal band used.

AF	Spectral Functions
Ψ_1	$\eta_{1\lambda} = 0.00090\lambda^3 - 0.01638\lambda^2 + 0.04745\lambda + 0.27436$ $\xi_{1\lambda} = 0.00032\lambda^3 - 0.06148\lambda^2 + 1.2021\lambda - 6.2051$ $\chi_{1\lambda} = 0.00986\lambda^3 - 0.23672\lambda^2 + 1.7133\lambda - 3.2199$ $\varphi_{1\lambda} = -0.15431\lambda^3 + 5.2757\lambda^2 - 60.1170\lambda + 229.3139$
Ψ_2	$\eta_{2\lambda} = -0.02883\lambda^3 + 0.87181\lambda^2 - 8.82712\lambda + 29.9092$ $\xi_{2\lambda} = 0.13515\lambda^3 - 4.1171\lambda^2 + 41.8295\lambda - 142.2782$ $\chi_{2\lambda} = -0.22765\lambda^3 + 6.8606\lambda^2 - 69.2577\lambda + 233.0722$ $\varphi_{2\lambda} = 0.41868\lambda^3 - 14.3299\lambda^2 + 163.6681\lambda - 623.5300$
Ψ_3	$\eta_{3\lambda} = 0.00182\lambda^3 - 0.04519\lambda^2 + 0.32652\lambda - 0.60030$ $\xi_{3\lambda} = -0.00744\lambda^3 + 0.11431\lambda^2 + 0.17560\lambda - 5.4588$ $\chi_{3\lambda} = -0.00269\lambda^3 + 0.31395\lambda^2 - 5.5916\lambda + 27.9913$ $\varphi_{3\lambda} = -0.07972\lambda^3 + 2.8396\lambda^2 - 33.6843\lambda + 132.9798$

Taking into account that this work used band 10 of Landsat 8 and that its average wavelength was 10.8 μm, the atmospheric functions are defined as

$$\begin{bmatrix} \psi_1 \\ \psi_2 \\ \psi_3 \end{bmatrix} = \begin{bmatrix} 0.0099976 & 0.00966064 & 0.09347952 & 1.02178928 \\ -0.05327456 & -0.4880672 & -1.4640128 & 0.06216416 \\ -0.05216976 & 0.39854112 & 0.83252272 & -0.02393664 \end{bmatrix} \begin{bmatrix} W^3 \\ W^2 \\ W \\ 1 \end{bmatrix}. \tag{9}$$

According to [17], the most important source of error in single-channel algorithms (in general, as regards the single-channel 1 and single-channel 2) is the introduction of the atmospheric effects, which leads to an error in the LST between 0.2 K and 0.7 K, and the uncertainty of the emissivity of the earth's surface, which produces an additional error in the surface temperature between 0.2 K and 0.4 K.

2. Methods

Once the most recommended methods for calculating LST by means of satellite images from only one thermal band were determined from a theoretical point of view, their evaluation was carried out in order to determine the most appropriate conditions for the application of each of them. To do this, throughout this section we proceed to the automation of the processes and the visualization of the results making combined use of the following two tools with great potential: Matlab® as a programming language for process automation, and QGIS® as a Geographic Information System for geospatial data processing. As a result of this combination, it was possible to perform an evaluation of the different methods mentioned, both from a numerical and a visual point of view. The products offered by NASA called analysis ready data (ARD) were considered as reference for the evaluation of each method under study in order to check their viability regarding the most official temperature product.

2.1. Landsat Analysis Ready Data (ARD)

ARD data was published in 2018 and created by NASA. Their bases were Landsat Level-1 products, including TOA (Top-Of-Atmosphere) reflectance, satellite brightness temperature, surface reflectance, and provisional terrestrial surface temperature.

Landsat ARD LST products are currently only available for the US. Images from the continental United States and Hawaii are generated in the Albers Equal Area (AEA) conical cartographic projection, using the WGS84 (World Geodetic System 1984) as datum.

Each ARD LST product has a spatial resolution of thirty meters, just like the original Landsat 8 products, but the size is smaller. Landsat ARD LST has 5000 × 5000 pixels versus approximately 6300 × 6000 pixels in the other products from Landsat 8.

The ARD LST products are different from those calculated in this article, mainly due to the processing procedure. Regarding the method for atmospheric correction of the optical spectrum, Landsat ARD generates surface reflectance using the Landsat Surface Reflectance Code, which uses the coastal spray band, MODIS auxiliary weather data, and a unique model of radiative transfer [32], while this paper implemented DOS 1 atmospheric correction [17], based on the MODIS atmospheric water content product. In addition, ARD LST products are generated using ASTER GED (Global-Emissivity Dataset) for surface emissivity and MODTRAN simulations powered by the atmosphere proposed by the NARR reanalysis [21], while the single-channel approaches used in the combined strategy retrieve surface emissivity by the NDVI threshold method to calculate surface emissivity.

2.2. LST Retrieval Methods: Evaluation and Comparison

The objective of the evaluation was to determine if the final result of each method, that is, the LST value obtained, approximated the value considered as reference. As mentioned before, the provisional surface temperature image of ARD was considered as reference.

For this comparison, sample images were randomly selected from locations distributed as homogeneously as possible in the USA and on different types of soil, including cases studies of desert, urban, crop, and forestry areas (Figure 3), taking into account case studies both in warm and cold seasons (Table 2). The images were cut in order to avoid the presence of urban areas, the particularities of which regarding temperature distribution and emission of thermal infrared radiation made necessary the adaptation of the existing LST retrieval methods [33,34].

Figure 3. Map of the USA with the points of the sample areas selected for the study. Red: crop areas, yellow: desert areas, green: forest areas, and blue: urban areas.

Table 2. List of dates and images in Figure 3.

Area Type	ID	Warm Season	Cold Season	Size (Pixels)
Crop area	1	A	B	1366 × 1425
	5	C	D	997 × 605
	9	E	F	856 × 982
Forest area	2	G	H	2674 × 2973
	6	I	J	993 × 1005
	10	K	L	736 × 572
Desert area	3	M	N	2053 × 1213
	7	O	P	831 × 1136
	11	Q	R	847 × 591
Urban area	4	S	T	1593 × 1436
	8	U	V	973 × 905
	12	W	X	299 × 175

This means that three different locations and two different dates are studied for each area. For this, 72 Landsat 8 images (24 sets of bands 4, 5 and 10) and their metadata will be downloaded. In addition, 24 MODIS water vapor products and the corresponding 24 ARD LST products are required for the study. Dates selected where those with the lowest percentage of cloudiness possible (below 2%).

Tables 3 and 4 show the numerical results obtained from the comparison between ARD LST products and the LST images resulting from the application of single-channel 1 and single-channel 2 methods. RMSE was calculated per pixel for each image resulting from both methods. Then, the mean RMSE was calculated per image and for the pixels of all images from the same method.

Table 3. Results of the mean square error between the analysis ready data (ARD) LST products and the different methods of LST retrieval in warm season.

		Crop Area			Forest Area			
		A	**C**	**E**	**G**	**I**	**K**	**Mean RMSE (K; %)**
W (g/cm^2)		2.94	1.25	5.03	2.57	1.89	1.79	
LST (K)		311.28	311.27	304.60	302.47	303.26	302.22	
Method and RMSE (K)	Single-Channel I	1.15	1.07	4.08	0.76	0.86	0.75	1.44 K; 0.47%
	Single-Channel II	1.62	2.06	11.34	1.04	1.54	1.45	3.17 K; 1.04%
		Desert Area			Urban Area			
		M	**O**	**Q**	**S**	**U**	**W**	**Mean RMSE (K; %)**
W (g/cm^2)		2.03	1.61	2.84	3.16	1.77	1.96	
LST (K)		314.32	327.83	327.02	301.92	326.37	303.91	
Method and RMSE (K)	Single-Channel I	0.81	1.44	6.04	2.31	0.58	1.18	2.06 K; 0.65%
	Single-Channel II	2.13	1.98	10.82	1.88	3.07	1.25	3.52 K; 1.11%
						Single-ChannelI		**1.75 K; 0.56%**
						Single-ChannelII		**3.35 K; 1.07%**

Table 4. Results of the mean square error between the ARD LST products and the different methods of LST retrieval in cold season.

		Crop Area			Forest Area			
		B	**D**	**F**	**H**	**J**	**L**	**Mean RMSE (K; %)**
W (g/cm^2)		1.65	0.46	1.28	1.58	0.71	1.52	
LST (K)		294.50	285.72	296.66	291.65	285.23	300.39	
Method and RMSE (K)	Single-Cha I	1.71	1.18	0.32	1.68	0.82	0.53	1.04 K; 0.36%
	Single-Cha II	0.48	0.45	1.71	0.30	0.76	1.63	0.89 K; 0.30%
		Desert Area			Urban Area			
		N	**P**	**R**	**T**	**V**	**X**	**Mean RMSE (K; %)**
W (g/cm^2)		0.57	1.02	1.19	1.29	1.06	0.83	
LST (K)		287.66	297.62	294.17	282.84	294.16	285.63	
Method and RMSE (K)	Single-Cha I	1.23	1.98	1.27	2.07	1.56	0.81	1.49 K; 0.51%
	Single-Cha II	0.32	0.44	0.62	0.90	0.39	0.77	0.57 K; 0.20%
						Single-ChannelI		**1.26 K; 0.43%**
						Single-ChannelII		**0.73 K; 0.25%**

For each sample area, LST was calculated using the different methods considered for this work (single-channel 1 and 2), calculating the difference with the ARD LST product, and obtaining its root mean square error. The surface temperatures and average water vapor content of each area were also indicated.

2.3. Determination of Conditions for the Optimal Application of the Methods

The results obtained in Tables 3 and 4 were sorted according to the average water vapor content and the methods with better and worse results, as seen in Table 5.

Table 5. LST retrieval methods in the thermal spectrum that are closest to the results of ARD LST products for the case studies. Images are sorted by the average water vapor content MODIS of each image.

Mean W Range (g/cm²)	Number of Images	Best Methodology	
<1.0	4	Single-Channel II	
1.0–1.2	3	Single-Channel II	
1.2–1.4	3	Single-Channel II (2)	Single-Channel I (1)
1.4–1.6	2	Single-Channel II (1)	Single-Channel I (1)
1.6–1.8	4	Single-Channel II (3)	Single-Channel I (1)
1.8–2.0	2	Single-Channel I	
>2.0	6	Single-Channel I	

The results could also be ordered taking into account their average terrestrial surface temperature, as shown in Table 6 and Figure 4.

Table 6. LST retrieval methods in the thermal spectrum that are closest to the results of ARD LST products for the case studies. Images are sorted by the average surface temperature ARD of each case study.

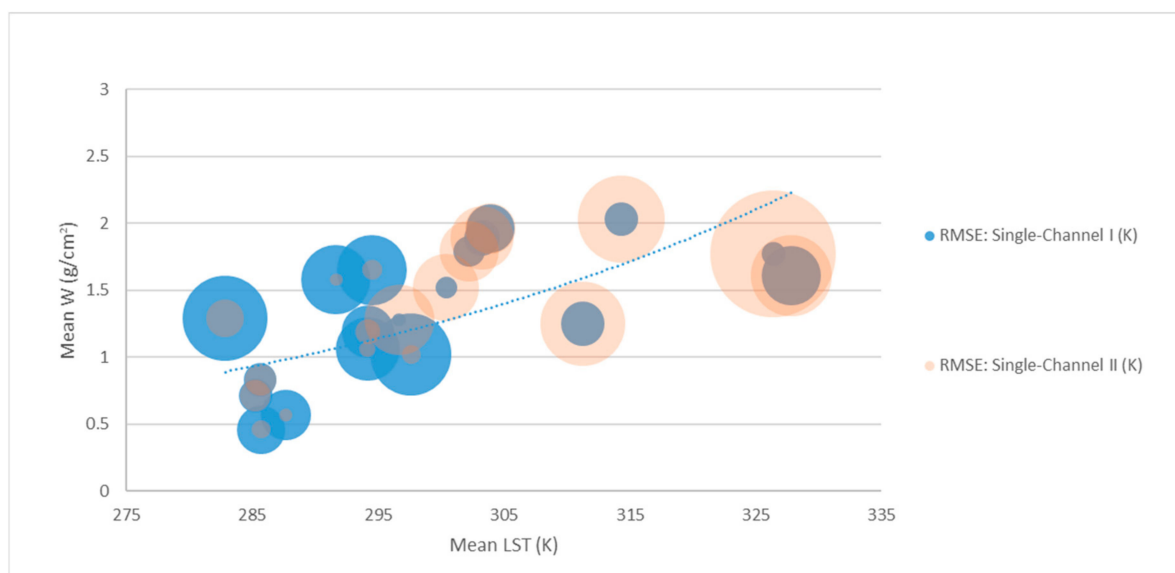| Mean LST Range (K)	Number of Images	Best Methodology	
<290	5	Single-Channel II	
290–295	4	Single-Channel II	
295–300	2	Single-Channel II (1)	Single-Channel I (1)
300–302	2	Single-Channel II (1)	Single-Channel I (1)
302–304	4	Single-Channel I	
>304	7	Single-Channel I	

Figure 4. Correlation between RMSE, LST, and average water vapor (W) content values.

Analyzing Tables 5 and 6 and Figure 4, the following conclusions could be reached. In the case of water vapor content, the results are as follows:

For water vapor content below 1.2 g/cm^2, the most approximate method compared to the results of NASA is the single-channel 2.

For water vapor content greater than 1.8 g/cm^2, the most approximate method is the single-channel 1.

For intermediate water vapor content values, the results vary between both methods.

The same happens if the analysis focuses on the surface temperature, as follows:

- For surface temperatures less than 295 K the most approximate method is single-channel 2.
- For temperatures greater than 302 K the closest method is single-channel 1.
- For intermediate values there is also variation.

The analysis of Tables 3 and 4 verified that, as a general rule, the higher the temperature, the higher the humidity, so that the characteristics necessary for the choice of the method are shared, the results of which are the most similar to those of the ARD LST products. With this information the combined strategy can be developed.

3. Results: Combined Strategy

Tables 5 and 6 show a trend in the results; for images acquired with high levels of water vapor content (1.8 g/cm^2), the most accurate method was single-channel 1 (assuming as more accurate the results that were closer to the values of the ARD LST products). However, when water vapor content was low (1.2 g/cm^2), the best method for LST computation was single-channel 2. It should be noted that the results presented high RMSE in cases where water vapor content was very high. This fact goes in coherence with studies such as [13], where results of LST when water vapor content was over 2.5 g/cm^2 were considered as not reliable. For intermediate values of water vapor content, no clear trend was found, with the best results oscillating between single-channel 1 and single-channel 2 methods.

Taking into account the results of the analysis, a combined strategy was developed that analyzed the image and computed LST pixel per pixel, according to the rule shown in Figure 5.
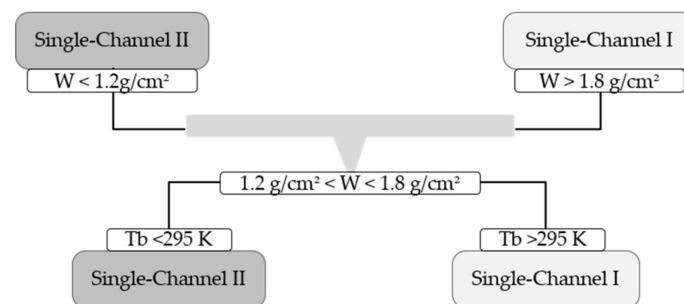

Figure 5. Logic followed by the "combined strategy" developed.

Thus, the first parameter under study was water vapor content (W), with the following decision-rule:

W > 1.8 g/cm^2: single-channel 1 method,

W < 1.2 g/cm^2: single-channel 2 method.

For intermediate values of W (between 1.2 and 1.8 (1.8 g/cm^2), the second parameter under study was satellite brightness temperature (Tb), which was closely related to LST. The logic applied was the following:

Tb > 295 K: single-channel 1 method,

Tb ≤ 295 K: single-channel 2 method.

In this way, the combined strategy consisted of an adaptive pixel-based LST retrieval methodology. Thus, the strategy analyzed the TIR image from which LST values needed to be retrieved, pixel by pixel. For each pixel, the water vapor content was analyzed, and the single-channel 1 or single-channel 2 method was used for the computation of LST. If the water vapor content was not decisive (that is, the value was between 1.2 and 1.8 g/cm^2), then the surface temperature was studied. Since the study was made pixel-by-pixel, both single-channel 1 and single-channel 2 could be applied in the same image, in different pixels each.

The combined strategy was subjected to both quantitative and visual evaluations, with the aim of determining its performance.

4. Discussion

4.1. Quantitative Evaluation

The results of LST obtained with the combined strategy were compared to ARD LST products considered as reference product.

This comparison was performed through the automation of the image processing and the application of the combined strategy in Matlab®. The images used for the validation of the combined strategy were the sample of 24 images used in the previous sections of the paper. Results are shown in Tables 7–10.

Table 7. Results of root mean square error (RMSE) of the combined strategy with respect to ARD LST products in crop areas.

	Crop Area					
	A	**B**	**C**	**D**	**E**	**F**
RMSE best methodology (K)	1.15	0.48	1.07	0.45	4.08	0.32
RMSE combined strategy (K)	1.14	0.49	1.18	0.45	4.08	1.56
W (g/cm^2)	2.94	1.65	1.25	0.46	5.03	1.28
LST (K)	311.28	294.50	311.27	285.72	304.60	296.66

Table 8. Results of root mean square error (RMSE) of the combined strategy with respect to ARD LST products in forest areas.

	Forest Area					
	G	**H**	**I**	**J**	**K**	**L**
RMSE best methodology (K)	0.76	0.30	0.86	0.76	0.75	0.53
RMSE combined strategy (K)	0.76	0.32	0.86	0.76	0.75	0.54
W (g/cm^2)	2.57	1.58	1.89	0.71	1.79	1.52
LST (K)	302.47	291.65	303.26	285.23	302.22	300.39

Table 9. Results of root mean square error (RMSE) of the combined strategy with respect to ARD LST products in desert areas.

	Desert Area					
	M	**N**	**O**	**P**	**Q**	**R**
RMSE best methodology (K)	0.81	0.32	1.44	0.44	6.04	0.62
RMSE combined strategy (K)	0.81	0.32	1.44	0.45	6.04	0.63
W (g/cm^2)	2.03	0.57	1.61	1.02	2.84	1.19
LST (K)	314.32	287.66	327.83	297.62	327.02	294.17

Table 10. Results of root mean square error (RMSE) of the combined strategy with respect to ARD LST products in urban areas.

	Urban Area					
	S	**T**	**U**	**V**	**W**	**X**
RMSE best methodology (K)	1.88	0.90	0.58	0.39	1.18	0.77
RMSE combined strategy (K)	2.31	0.90	0.58	0.39	1.18	0.77
W (g/cm^2)	3.16	1.29	1.77	1.06	1.96	0.83
LST (K)	301.92	282.84	326.37	294.16	303.91	285.63

Results showed that the mean RMSE for all areas of the combined strategy was 1.20 K, while the mean RMSE of the optimal single-channel method for each image were 1.51 K and 2.04 K, for single-channel 1 and 2, respectively. Thus, the combined strategy implied a mean improvement of 20% and 41%, respectively.

4.2. Visual Evaluation

Provided that both the inputs and the outputs of the computation of LST from satellite imagery present image-nature, visual analysis of the results is required. This way, for example, the coincidence of location of the coldest/hottest areas can be detected, as well as the identification of the magnitude of the error (the same RMSE can be obtained for a small difference for all pixels in the image, and for a large difference for a small number of pixels, and this can be identified visually). Tables 7–10 show results of improvement, worsening, or selection of the wrong method. These are all evaluated visually in this section.

Figure 6 shows an image where the combined strategy presents the same RMSE as the optimal single-channel method, which corresponds to image N from a desert area.
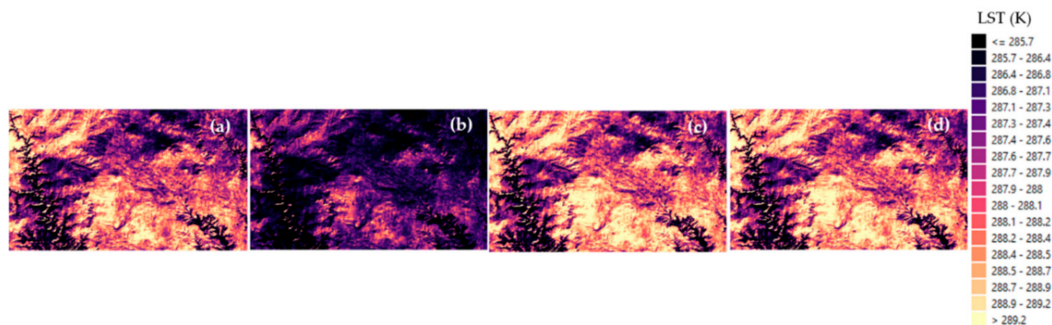

Figure 6. LST images of image N, from a desert area, with w = 0.57 g/cm^2 and mean LST = 287.66 K according to ARD product: (**a**) ARD LST product, (**b**) image calculated with single-channel 1 method, (**c**) image calculated with single-channel 2 method, (**d**) image obtained with the combined strategy.

Figure 6 shows that images resulting from the single-channel 2 method (c) and the combined strategy (d) are equal. In addition, the images resulting from these methods are more visually similar to the ARD LST product (a) than the image resulting from the single-channel 1 method (b). This similarity can also be evaluated through the generation of images of difference of temperatures, as shown in Figure 7.

Figure 7. Images of difference of LST from the reference (ARD LST product) and (**a**) single-channel 1 method, (**b**) single-channel 2 method, and (**c**) combined strategy, for image N from a desert area.

Next, a case study where the combined strategy does not improve the results of the best single-channel method is shown. This case corresponds to image C, corresponding to a crop area. According to Table 3, the best method is single-channel 1, with an RMSE of 1.07 K. Figures 8 and 9 show that the RMSE of the combined strategy is higher than that of single-channel 1, but results are better than those from single-channel 2 (2.06 K).
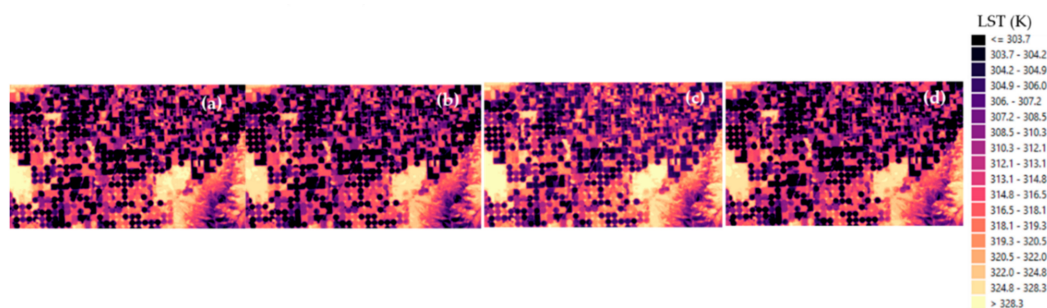
Figure 8. LST images of image C, from a crop area, with w = 1.25 g/cm^2 and mean LST = 311.27 K according to ARD image: (**a**) ARD LST product, (**b**) image calculated with single-channel 1 method, (**c**) image calculated with single-channel 2 method, (**d**) image obtained with the combined strategy.

Figure 8 shows no radical difference between temperatures obtained with the single-channel 1 method (b) and the combined strategy (d). It is also not clear that the single-channel 2 method is the worst (c). Figure 9 shows this comparison more clearly. Figure 9 shows that the RMSE of the combined strategy is a combination of the RMSE of single-channel 1 and 2 methods. If the image of water vapor content is studied (Figure 9d), the coincidence of the pixels with lower vapor content with the RMSE of the single-channel 2 method is unequivocally identified. Thus, this image is a clear example of the pixel-by-pixel analysis basis of the combined strategy.
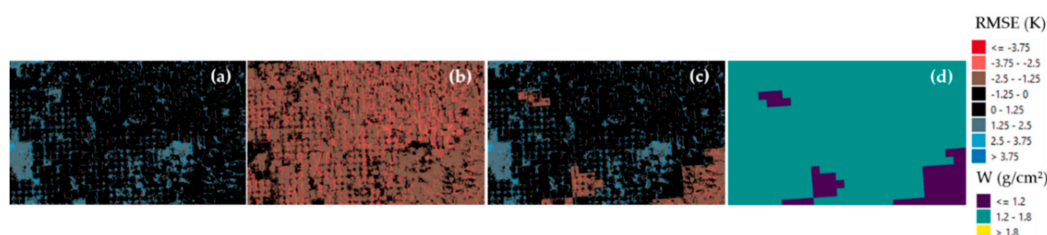

Figure 9. Images of difference of LST from the reference (ARD LST product) and (**a**) single-channel 1 method, (**b**) single-channel 2 method, and (**c**) combined strategy, for image C from a crop area; (**d**) is the image of water vapor content values.

Figure 10 shows a case study where the combined strategy presents poor results, with mean RMSE over 2 K. The reason for this is that the single-channel method did not present accurate results (Figure 10b,c). This is due to the high water vapor content in the area of over 2.5 g/cm^2. This case study serves as a confirmation that values of water vapor content over 2.5 g/cm^2 are the limit for the application of the combined strategy proposed in this paper.
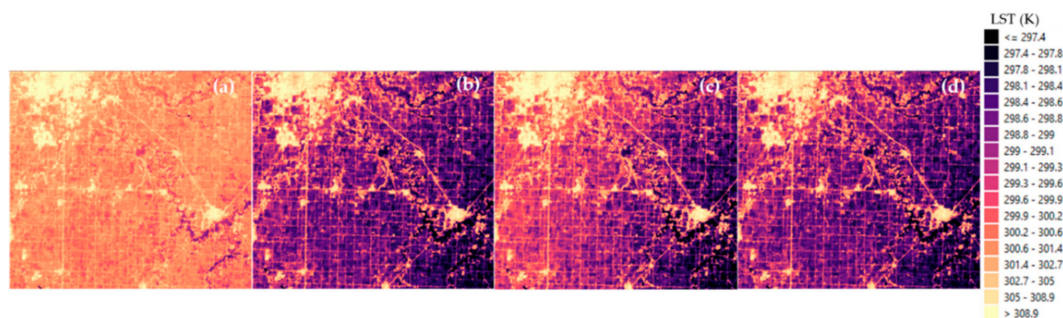
Figure 10. LST images of image S, from a urban area, with w = 3.16 g/cm^2 and mean LST = 301.92 K according to ARD image: (**a**) ARD LST product, (**b**) image calculated with single-channel 1 method, (**c**) image calculated with single-channel 2 method, (**d**) image obtained with the combined strategy.

4.3. Application of Combined Strategy to Other Sensors

The combined strategy was developed and tested with images from the Landsat 8 satellite. However, its application is not limited to this satellite, being usable by other satellites that incorporate the visible, near infrared, and thermal infrared bands needed. In fact, original single-channel methods were implemented for satellites earlier than Landsat 8 [12,18,21].

Some studies focus on the computation of LST from other satellites such as ASTER [35,36]. These use the same single-channel methods analyzed in this paper, adapted to the wavelength of the bands in ASTER. This implies that the combined strategy can also be applied to ASTER images, with the corresponding adaptation of the algorithms.

In order to evaluate the applicability of the combined strategy to the retrieval of LST from ASTER images, the resulting LST image was compared to AST 08V003 product [37], which is the ARD LST generated by ASTER. The results obtained are shown in Table 11. AST 08V003 was used as reference in this case in order to make a proper comparison of the combined strategy proposed with the official product generated from the same raw data, avoiding the effect of the different day and hour of acquisition that would have been present if the reference had been the ARD LST product from Landsat 8. In this case, the validity of the combined strategy proposed implies a simplification of the methodology for LST retrieval, since the official methodology used is a multi-channel temperature–emissivity separation (TES) algorithm that requires a minimum of three bands in the TIR spectrum [38], and the strategy proposed only needs one TIR band.

Table 11. Results of root mean square error between ASTER 08V003 images and single-channel 1, single-channel 2, and combined strategy.

	Crop/Urban/Forest Area
	23/05/18
RMSE Single-Channel I (K)	1.74
RMSE Single-Channel II (K)	2.49
RMSE Combined Strategy (K)	1.74
W (g/cm^2)	2.31
LST (K) AST 08V003	304.47

In this case, the combined strategy presents the same RMSE as the single-channel 1 method, consequently not worsening the results of none of the existing methods, and improving the results by 30% with regard to the worst method (Figure 11 shows the visual results of the application of each method).
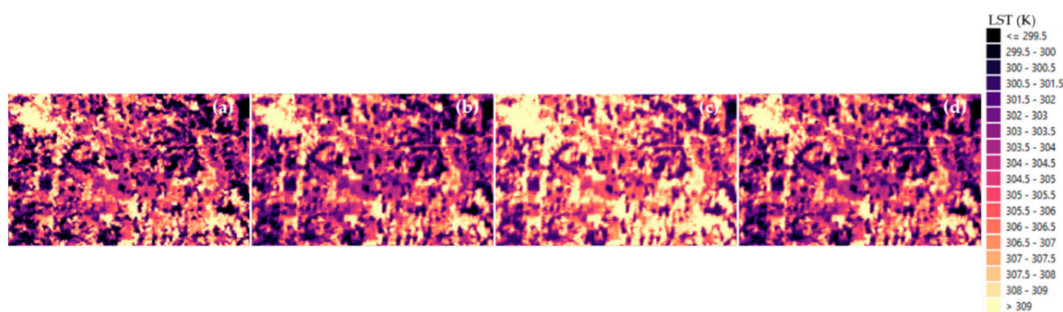
Figure 11. LST images from the ASTER TIR image, with w = 2.31 g/cm^2 and mean LST = 304.47 K according to ARD LST product: (**a**) AST 08V003 product, (**b**) image calculated with single-channel 1 method, (**c**) image calculated with single-channel 2 method, (**d**) image obtained with the combined strategy.

The results of the analysis of the application of the combined strategy to ASTER images show that the method presents better results than the methodologies officially used, also for satellites other than Landsat.

5. Conclusions

The need to perform global measurements of LST was the main reason for the evaluation of the viability of satellite imagery for the task. However, the number of methodologies available for the task is constantly increasing, the single-channel methods being the ones most widely used. The reason for the latter is that single-channel methods allow the computation of LST from one image in the thermal infrared band only, provided that a set of additional parameters (atmospheric conditions, surface emissivity) is previously known or calculated, in such a way that the method can be applied to any satellite with at least one thermal infrared band and is not limited to those sensors including several acquisitions within the band. However, existing single-channel methods differ from each other by the procedures applied to obtain the required additional parameters, which can also be different for each method, and there is no clear determination of the most precise and accurate method for each situation.

Thus, this paper performed an analysis of the most widely used single-channel methods, resulting in the development of a "combined strategy". The combined strategy uses both single-channel 1 (second grade polynomial including water vapor content (W) as parameter) and single-channel 2 (third grade polynomial with water vapor content as parameter) methods. The combined strategy was developed by comparing the LST images resulting from each method (single-channel 1 and 2) with the official ARD LST images for each sensor (Landsat and ASTER), which were considered as reference products. Results showed that when W was over 1.8 g/cm^2 the best method was single-channel 1, while when W was below 1.2 g/cm^2 single-channel 2 generated better results. For values of W between 1.2 and 1.8 g/cm^2, satellite brightness temperature (Tb) was the parameter that influenced the performance of the LST computation methods. Thus, the analysis performed showed that Tb over 295 K was better dealt with using the single-channel 1 method, while Tb below 295 K had better results with the single-channel 2 method.

Thus, the combined strategy developed in this work consists of the automatic application of one method (single-channel 1 or single-channel 2) for each pixel in the satellite images, according to the different values of W and Tb in them. The evaluation of a sample of 24 images showed that the RMSE of the combined method was 1.20 K, and the RMSE of single-channel 1 and single-channel 2 methods were 1.51 K and 2.04 K, respectively. This means that the combined strategy implies an improvement of 20% and 41% regarding each single-channel method (1 and 2). However, the performance of the combined strategy can be worse in the case of W values over 2.5 g/cm^2. Future work will deepen the analysis of the most extreme situations regarding humidity in order to determine and develop better methods for the computation of LST.

6. Patents

The developments of this paper have been subjected to Intellectual Property rights registration, in the name of the Universidad de Salamanca (Spain), with reference SA-113-19. The name of the software is TEMISAT—Temperature from Satellite Image.

Author Contributions: Conceptualization, S.L. and S.D.P.; methodology, M.S.-A.; software, P.A.-A.; validation, M.S.-A., P.A.-A., and S.L.; formal analysis, M.S.-A. and S.D.P.; investigation, P.A.-A.; resources, S.L.; writing—original draft preparation, P.A.-A.; writing—review and editing, M.S.-A.; supervision, S.L.; project administration, S.L.; funding acquisition, S.L. All authors have read and agreed to the published version of the manuscript.

Conflicts of Interest: The authors declare no conflict of interest.

References

1. Maurer, J.M.; Schaefer, J.M.; Rupper, S.; Corley, A. Acceleration of ice loss across the Himalayas over the past 40 years. *Sci. Adv.* **2019**, *5*, EAAV7266. [CrossRef]
2. Dangendorf, S.; Hay, C.; Calafat, F.M.; Marcos, M.; Piecuch, C.G.; Berk, K.; Jensen, J. Persistent acceleration in global sea-level rise since the 1960s. *Nat. Clim. Chang.* **2019**, *9*, 705–710. [CrossRef]
3. Ministry of Agriculture and Fishing, Food and Environment, Government of Spain. Summary Report on the Situation of Hydrological Drought. Catalogue of Publications of the General State Administration. 2017. Available online: https://www.mapa.gob.es/ministerio/pags/biblioteca/revistas/pdf_SSR/1707-pdf_SSR_SSR_2017_jul.pdf (accessed on 13 November 2019).
4. Ministry of Agriculture and Fishing, Food and Environment, Government of Spain. Summary Report on the Climatological Year. Catalogue of Publications of the General State Administration. 2017. Available online: http://www.aemet.es/documentos/es/serviciosclimaticos/vigilancia_clima/resumenes_climat/anuales/res_anual_clim_2017.pdf (accessed on 16 December 2019).
5. Julien, Y.; Sobrino, J.A.; Verhoef, W. Changes in land surface temperatures and NDVI values over Europe between 1982 and 1999. *Remote Sens. Environ.* **2006**, *103*, 43–55. [CrossRef]
6. Marcos, E.; Fernández-García, V.; Fernández-Manso, A.; Quintano, C.; Valbuena, L.; Tárrega, R.; Luis-Calabuig, E.; Calvo, L. Evaluation of composite burn index and land surface temperature for assessing soil burn severity in mediterranean fire-prone pine ecosystems. *Forest* **2018**, *9*, 494. [CrossRef]
7. Maffei, C.; Alfieri, S.; Menenti, M. Relating spatiotemporal patterns of forest fires burned area and duration to diurnal Land Surface Temperature anomalies. *Remote Sens.* **2018**, *10*, 1777. [CrossRef]
8. Mia, M.B.; Fujimitsu, Y.; Nishijima, J. Monitoring of thermal activity at the Hatchobaru-Otake geotermal area in Japan using multi-source satellite images with comparisons of methods, and solar and seasonal effects. *Remote Sens.* **2018**, *10*, 1430. [CrossRef]
9. Darge, Y.M.; Hailu, B.T.; Muluneh, A.A.; Kidane, T. Detection of geothermal anomalies using Landsat 8 TIRS data on Tulu Moye geothermal prospect, Main Ethiopian Rift. *Int. J. Appl. Earth Obs. Geoinf.* **2019**, *74*, 16–26. [CrossRef]
10. United Nations, The Sustainable Development Goals Report 2019, New York. Available online: https://unstats.un.org/sdgs/report/2019/The-Sustainable-Development-Goals-Report-2019.pdf (accessed on 13 November 2019).
11. Eludoyin, A.O.; Omotoso, I.; Eludoyin, O.M.; Popoola, K.S. Remote sensing technology for evaluation of variations in land surface temperature, and case study analysis from Southwest Nigeria. In *Geospatial Challenges in the 21st Century*; Springer: Cham, Switzerland, 2019; pp. 151–170.
12. Li, Z.L.; Tang, B.H.; Wu, H.; Ren, H.; Yan, G.; Wan, Z.; Sobrino, J.A. Satellite-derived land surface temperature: Current status and perspectives. *Remote Sens. Environ.* **2013**, *131*, 14–37. [CrossRef]
13. Snyder, W.C.; Wan, Z.; Zhang, Y.; Feng, Y.Z. Classification-based emissivity for land surface temperature measurement from space. *Int. J. Remote Sens.* **1998**, *19*, 2753–2774. [CrossRef]

14. Barducci, A.; Pippi, I. Temperature and emissivity retrieval from remotely sensed images using the grey body emissivity method. *IEEE Trans. Geosci. Remote Sens.* **1996**, *34*, 681–695. [CrossRef]

15. Gillespie, A.R.; Rokugawa, S.; Hook, S.J.; Matsunaga, T.; Kahle, A.B. *Temperature/Emissivity Separation Algorithm Theoretical Basis Document, Version 2.4.; ATBD Contract NAS5-31372*; NASA: Washington, DC, USA, 1999.

16. Mao, K.; Shi, J.; Tang, H.; Li, Z.L.; Wang, X.; Chen, K.S. A neural network technique for separating land surface emissivity and temperature from ASTER imagery. *IEEE Trans. Geosci. Remote Sens.* **2007**, *46*, 200–208. [CrossRef]

17. Jiménez-Muñoz, J.C.; Sobrino, J.A.; Skoković, D.; Mattar, C.; Cristóbal, J. Land surface temperature retrieval methods from Landsat-8 thermal infrared sensor data. *IEEE Geosci. Remote Sens. Lett.* **2014**, *11*, 1840–1843. [CrossRef]

18. Cristóbal, J.; Jiménez-Muñoz, J.; Prakash, A.; Mattar, C.; Skoković, D.; Sobrino, J. An improved single-channel method to retrieve land surface temperature from the Landsat-8 Thermal Band. *Remote Sens.* **2018**, *10*, 431. [CrossRef]

19. Sobrino, J.A.; Li, Z.L.; Stoll, M.P.; Becker, F. Multi-channel and multi-angle algorithms for estimating sea and land surface temperature with ATSR data. *Int. J. Remote Sens.* **1996**, *17*, 2089–2114. [CrossRef]

20. Tanre, D.; Holben, B.N.; Kaufman, Y.J. Atmospheric correction algorithm for NOAA-AVHRR products: Theory and application. *IEEE Trans. Geosci. Remote Sens* **1992**, *30*, 231–250. [CrossRef]

21. Yu, X.; Guo, X.; Wu, Z. Land surface temperature retrieval from Landsat 8 TIRS—Comparison between radiative transfer equation-based method, split window algorithm and single channel method. *Remote Sens.* **2014**, *6*, 9829–9852. [CrossRef]

22. Dwyer, J.; Roy, D.; Sauer, B.; Jenkerson, C.; Zhang, H.; Lymburner, L. Analysis ready data: Enabling analysis of the Landsat archive. *Remote Sens.* **2018**, *10*, 1363.

23. ESA Sentinel Online. Sentinel 3—SLSTR User Guide. Available online: https://earth.esa.int/web/sentinel/user-guides/sentinel-3-slstr/product-types/level-2-lst (accessed on 16 December 2019).

24. Abrams, M.; Tsu, H.; Hulley, G.; Iwao, K.; Pieri, D.; Cudahy, T.; Kargel, J. The Advanced Spaceborne Thermal Emission and Reflection Radiometer (ASTER) after fifteen years: Review of global products. *Int. J. Appl. Earth Obs. Geoinf.* **2015**, *38*, 292–301. [CrossRef]

25. Cook, M.; Schott, J.; Mandel, J.; Raqueno, N. Development of an operational calibration methodology for the Landsat thermal data archive and initial testing of the atmospheric compensation component of Land Surface Temperature (LST) product from the archive. *Remote Sens.* **2014**, *6*, 11244–11266. [CrossRef]

26. Malakar, N.; Hulley, G.; Hook, S.; Laraby, K.; Cook, M.; Schott, R.J. An operational Land Surface Temperature product for Landsat thermal data: Methodology and validation. *IEEE Trans. Geosci. Remote Sens.* **2018**, *99*, 1–19. [CrossRef]

27. Wang, L.; Lu, Y.; Yao, Y. Comparison of three algorithms for the retrieval of Land Surface Temperature from Lansat 8 images. *Sensors* **2019**, *19*, 5049. [CrossRef] [PubMed]

28. Ariza, A. Descripción y Corrección de Productos Landsat 8 LDCM. Versión 1.0. Instituto Geográfico Agustín Codazzi, Bogotá (Colombia). Available online: http://www.un-spider.org/sites/default/files/LDCM-L8.R1.pdf (accessed on 18 December 2019).

29. Jiménez-Muñoz, J.C.; Sobrino, J.A. A generalized single-channel method for retrieving land surface temperature from remote sensing data. *J. Geophys. Res. Atmos.* **2003**, *108*. [CrossRef]

30. Borbas, E.; Menzel, P.; Gao, B. *MODIS Atmosphere L2 Water Vapor Product*; NASA MODIS Adaptive Processing System, Goddard Space Flight Center: Greenbelt, MD, USA, 2015.

31. Coll, C.; Caselles, V.; Valor, E.; Niclòs, R. Comparison between different sources of atmospheric profiles for land surface temperature retrieval from single channel thermal infrared data. *Remote Sens. Environ.* **2012**, *117*, 199–210. [CrossRef]

32. Department of Interior, US Geological Survey. LANDSAT 8 SURFACE REFLECTANCE CODE (LASRC) PRODUCT GUIDE LSDS-1368 Versión 2.0, South Dakota. Available online: https://prd-wret.s3-us-west-2.amazonaws.com/assets/palladium/production/atoms/files/LSDS-1368_L8_SurfaceReflectanceCode-LASRC_ProductGuide-v2.pdf (accessed on 13 November 2019).

33. Guo, A.; Yang, J.; Xiao, X.; Xia, J.; Jin, C.; Li, X. Influences of urban spatial form on urban heat islands effects at the community level in China. *Sustain. Cities Soc.* **2020**, *53*, 101972. [CrossRef]

34. Lemus-Canovas, M.; Martín-Vide, J.; Moreno-García, M.C.; Lopez-Bustins, J.A. Estimating Barcelona's metropolitan daytime hot and cold poles using Landsat-8 Land Surface Temperature. *Sci. Tot. Environ.* **2020**, *699*, 134307. [CrossRef] [PubMed]
35. Jiménez-Muñoz, J.C.; Sobrino, J.A. A single-channel algorithm for land-surface temperature retrieval from ASTER data. *IEEE Geosci. Remote Sens. Lett.* **2009**, *7*, 176–179. [CrossRef]
36. Xiong, Y.; He, J.; Ma, N.; Ren, X.; Liu, C. Land surface temperature retrieval based on thermal infrared remotely sensed data of aster. *IOP Conf. Ser. Earth Environ. Sci.* **2019**, *300*, 022027. [CrossRef]
37. NASA/METI/AIST/Japan Spacesystems; U.S./Japan ASTER Science Team. ASTER Level 2 Surface Temperature Product. NASA EOSDIS Land Processes DAAC 2001. Available online: https://doi.org/10.5067/ASTER/AST_08.003 (accessed on 19 December 2019).
38. Gillespie, A.; Rokugawa, S.; Matsunaga, T.; Cothern, J.S.; Hook, S.; Kahle, A.B. A Temperature and Emissivity Separation algorithm for Advanced Spaceborne Thermal Emission and Reflection Radiometer (ASTER) images. *IEEE Geosci. Remote Sens.* **1998**, *36*, 1113–1126. [CrossRef]